Origin of multiplexing capabilities of multifrequency magnetic ratchets

Yuyu Ouyang,[1,*] Mukarram A. Tahir,[2] Daniel J. Lichtenwalner,[3] and Benjamin B. Yellen[1,2,†]

[1]*University of Michigan–Shanghai Jiao Tong University Joint Institute, Shanghai Jiao Tong University, Shanghai, People's Republic of China*

[2]*Department of Mechanical Engineering and Materials Science, Center for Biologically Inspired Materials and Material Systems, Duke University, Durham, North Carolina 27708, USA*

[3]*Department of Materials Science and Engineering, North Carolina State University, Raleigh, North Carolina 27606, USA*

Through a combination of theory, numerical simulation, and experiment, we investigate the motion of magnetic beads on the surface of a magnetic ratchet driven by multifrequency fields. Here, we focus on the influence of static forcing terms, which were not included in previous models, and we derive analytical models that show why the static forcing terms are responsible for inducing beads of two different sizes to move in opposite directions on the same ratchet potential. We begin our analysis with the simplest possible forcing model, and we show that the main effect of the static forcing terms is to delay the phase of flux reversal. From there, we move onto the full analysis and theoretically derive the phase range for which opposite motion among two different bead types is achieved. Based on these theoretical results, we conduct experimental investigations that explore the effects of bead size and static forcing coefficient on the direction of bead motion, which confirm most of the expected trends. These results shed light both on past experimental work both by ourselves and others, as well as elucidate the more general multiplexing capabilities of ratchets.

　　　　PACS number(s): 83.80.Hj, 05.45.Xt

I. INTRODUCTION

Brownian and deterministic ratchets have attracted considerable attention both as physical models for understanding biological mechanisms (e.g., molecular motors [1,2]) and as tools for channeling the flow of material, energy, and information. The term "ratchet" was originally used to describe the mechanism by which a gear wheel guides another mobile component via geometric matching of the spatial features in two opposing surfaces (i.e., gear teeth). In a more general sense, ratchet can refer to any time-modulated periodic potential energy landscape that is used to control various mobile components (particles) ranging from electrons [3], spins [4–7], atoms [8–10], as well as molecules, colloidal particles [11–20], and biological materials [15,17,18,20,21]. Time modulation of the landscape is typically accomplished with an external electric, optical, magnetic, acoustic, thermal, or fluidic source field and used to rectify one type of motion (e.g., external field rotation) into another type (e.g., particle translation) [15]. A rich display of synchronization has been observed in these systems resulting from the interplay between the periodicities of the underlying landscape and the various modes of excitation (monochromatic, multichromatic, impulse functions, white noise, etc.). Rectified particle flux in spatially asymmetric landscapes has been observed in systems such as colloidal and molecular motion inside asymmetric pores [13,21] and above asymmetric electric potentials [22,23], electron and atom motion in quantum ratchets [3,8,24], spin transport in superconductors [7], and many others. The ratchet effect has also been observed in landscapes that have time asymmetry instead of space asymmetry, such as spin vortex motion [4–6] cold atoms in optical ratchets [9,10], colloidal

particles in optical lattices [11,25], and superparamagnetic beads in magnetic lattices [14–16,19].

The work presented here was motivated by recent experimental observations [19,26], which have demonstrated the possibility of using multifrequency driving fields to achieve differential motion among two different types of superparamagnetic beads exposed to the same ratchet potential. In these experiments, it was shown that the phase difference between multifrequency driving fields could be used as a tuning parameter both to control the direction of bead motion and also drive beads of two different sizes in opposite directions; however, the reason why this multiplexing capability is possible was not known at the time. In our first attempt to explain this experimental behavior, we derived theoretical models that could predict the phase-modulated flux reversal as well as the necessary conditions required to achieve open trajectories vs closed trajectories; however, we were unable to identify the origin of the particle separation behavior (i.e., how the flux reversal depends on the size of the bead and the phase difference between the two driving frequencies) [26]. We speculated that this anomalous behavior could have its origins in the static forcing terms that were omitted in our simplified theoretical models; however, at that time these speculations were not grounded with a solid theoretical analysis.

In this article, we conduct a follow-up analysis which identifies that the role of the static forcing terms is to delay the phase at which beads experience flux reversal, and we further analyze how the flux reversal depends on the bead size, thereby opening up new insights into the design of more sensitive and multiplexed bead separation systems. In addition, we present experimental results which show the correct qualitative trends. There are some experimental observations that cannot be explained by our analytical model, such as the presence of a zero-velocity regime, since our model is based on a perturbation analysis. In numerical simulations, on the other hand, a zero-velocity region was found only for magnetic substrates that had spatial asymmetry in the magnetic pole

*ouyangyuyu@gmail.com
†yellen@duke.edu

distribution of the substrate. The main conclusion of our work is that static forcing terms are a viable explanation for the origin of differential motion among different bead types on the same ratchet. Thus, through the combination of theory, simulation, and experiment we show that it is possible to enable future improvements of magnetic separation systems.

The rest of this article is organized as follows: In Sec. II, we derive several theoretical models of increasing complexity, starting with the simplest model and moving to the most realistic one. In Sec. III, we present analytical and numerical simulation results which reveal the influence of the static forcing terms in delaying the phase of flux reversal. We describe the experimental methods in Sec. IV, and present the experimental results in Sec. V which show general agreement with the trends predicted by theory. We conclude with a short summary in Sec. VI and identify open questions.

II. THEORETICAL MODEL

Though some of this analysis has been presented in our prior works [26], for the sake of completeness we summarize the key points that govern the equations of motion of a superparamagnetic bead in a time-modulated periodic potential energy landscape. Through this discussion, we will highlight the origin of both the dynamic and static forcing terms, and show how their relative magnitude can be modulated.

Our experimental system consists of a square lattice of identical circular micromagnets with diameter d_m and period d, which are uniformly magnetized along the x direction. Square array patterns are chosen primarily for experimental convenience, since it allows the direction of magnetization to be controlled more easily within the two-dimensional (2D) plane. The most accurate description of the substrate pole distribution would consist of treating each uniformly magnetized micromagnet as having equivalent magnetic charges that vary sinusoidally around the micromagnet's perimeter according to $\sigma = \vec{M} \cdot \hat{n} = |\vec{M}| \cos \theta$, where σ is the magnetic pole density, $\vec{M}$ is the remanent magnetization, $\hat{n}$ is the surface normal of thin magnetic disks, and θ is the angle relative to the positive x direction. For simplification, we can approximate each micromagnet as having its magnetic pole distribution concentrated at its poles. Additionally, since we apply our external fields along the x and z directions, the symmetry along the y direction allows us to further simplify this system, in which case we ignore the charge density variation along the y direction. Conceptually, this charge distribution would be consistent with an array of infinitely long magnetic bars that are magnetized along their minor axes, as shown in Fig. 1. Although this pole distribution is not exactly the same as a square lattice of circular micromagnets, it allows for analytically tractable solutions to be obtained in one dimension.

When represented in Fourier space, the line charge array has a pole distribution of

$$\lambda(\xi_x) = 2\lambda_0 \sum_{n=\text{odd}}^{\infty} \cos(n\xi_x), \qquad (1)$$

where we use the shorthand notation $\xi_x = 2\pi x/d$, $d/d_m = 2$ in which the magnet diameter is half of the period length,
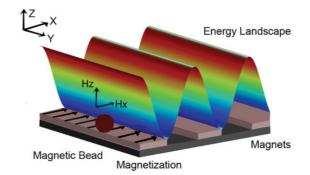

FIG. 1. (Color online) Schematic of the potential energy landscape of the bead exposed to a periodic array of micromagnets (approximated as a 1D array of infinitely long bar magnets) and external time-varying fields applied along the x and z directions. The bead is shown as a circle. The magnetization direction of the micromagnets is along the short axis.

and λ_0 is the magnetic line pole strength. From Eq. (1), the magnetic scalar potential of the substrate can be solved through separation of variables in Cartesian coordinates, and the magnetic field distribution is determined by taking the negative gradient of the scalar potential, leading to

$$\vec{H}_{\text{sub}} = -\lambda_0 \sum_{n=\text{odd}} e^{-n\xi_z} \{\hat{x} \, \sin(n\xi_x) + \hat{z} \, \cos(n\xi_x)\}. \qquad (2)$$

In addition to the static fields of the substrate, we also apply time-varying external driving fields, given by

$$\vec{H}_{\text{ext}} = H_{\text{ext}} \{\hat{x} \, \sin(\omega_x t) + \hat{z} \, \sin(\omega_z t + \varphi)\}, \qquad (3)$$

where ω_x and ω_z are the external driving frequencies along the x and z directions, respectively, and ϕ is the $t = 0$ phase difference between the two driving fields.

Superparamagnetic beads exposed to this potential energy landscape are modeled as point dipoles, which is a reasonable approximation when the field does not vary strongly across the particle's volume. The dipole moment of the bead is given by

$$\vec{m} = 3 \frac{\mu_p - \mu_f}{\mu_p + 2\mu_f} V \vec{H} = \bar{\chi} V \vec{H}, \qquad (4)$$

where V is the bead's volume, $\vec{H}$ is the total field at the bead's center, and μ_p and μ_f are the magnetic permeabilities of the bead and fluid, respectively. Since the surrounding fluid is water, we assume $\mu_f \approx \mu_0$, whereas the bead's permeability is given by $\mu_p = \mu_0(1 + \chi)$ and χ is the magnetic susceptibility, which depends on the bead's material properties. Using these assumptions, the force on a point dipole exposed to the micromagnetic ratchet and external time-varying fields is determined to be the sum of terms that are space-time dependent, and terms that are only spatially dependent:

$$\vec{F}(\xi_x, t) = \mu_0(\vec{m} \cdot \vec{\nabla})\vec{H}_{\text{tot}} = \vec{F}_d(\xi_x, t) + \vec{F}_s(\xi_x). \qquad (5)$$

The space-time-dependent terms arise from the external field's contribution to magnetizing the bead, whereas the purely space-dependent terms arise due to the substrate's contribution both to magnetizing the bead and providing the force through its field gradient.

The equations of motion for micrometer-sized colloidal particles (low Reynold's number) can be approximated by overdamped first order dynamics, in which the friction coefficient is assumed to be Stoke's drag on a sphere. Using dimensionless spatial coordinates, the velocity is given by

$$\dot{\xi}_x = \omega_0 \left[\sum_{n=\text{odd}} n e^{-2\pi n\beta} \{\cos(n\xi_x)\sin(\omega_x t) - \sin(n\xi_x)\sin(\omega_z t + \varphi)\} + \frac{\lambda_0}{H_{\text{ext}}} \sum_{n=\text{odd}} \sum_{m=\text{odd}} (n - m) e^{-2\pi(n+m)\beta} \sin(n\xi_x)\cos(m\xi_x) \right],$$

(6)

where $\omega_0 = 2\mu_0 \bar{\chi} \lambda_0 H_{\text{ext}}(2\pi\beta)^2/9\eta$ is a characteristic frequency that depends on the external system and bead properties, and $\beta = a/d$ represents the ratio of the bead radius, a, relative to the lattice period, d. Here, we assume that the bead's vertical position remains one bead radius above the substrate, since the force in the z direction is usually downward (attractive toward the substrate) and thus the z forces can be omitted, leading to a one-dimensional (1D) forcing model. In the following analysis we replace ξ_x with ξ since we are only concerned with the motion in one dimension. Equation (6) indicates that the relative strength of the static forcing terms (time independent) can be modulated by controlling the ratio of the substrate magnetization relative to the external field, which is explored here numerically and experimentally.

III. THEORETICAL RESULTS

Due to the complexity of Eq. (6), we begin by analyzing several limiting cases, and then build up to the complete analysis. In the following discussion, we will analyze the flux reversal properties as a function of the phase difference, static forcing terms, bead properties, and external driving frequencies.

Case I. $\lambda_0 \ll H_{\text{ext}}$. This approximation implies that the static forcing terms are negligible and here we start by considering only the first dynamic term in Eq. (6), leading to the following simplified dynamic model:

$$\dot{\xi} = \omega_0^* \{\cos(\xi)\sin(\omega_x t) - \sin(\xi)\sin(\omega_z t + \varphi)\}, \quad (7)$$

where $\omega_0^* = \omega_0 e^{-2\pi\beta}$. When the external driving frequencies ω_x and ω_z are much smaller than the characteristic frequency ω_0^*, the bead's motion approaches the adiabatic limit, and a direct analytical relationship can be obtained for the bead's velocity by setting Eq. (7) to equal zero [26], leading to

$$\tan(\xi) = \frac{\sin(\omega_x t)}{\sin(\omega_z t + \varphi)}. \quad (8)$$

A comparison of the analytical result (8) with numerical simulations of Eq. (7) using high resolution finite time difference technique shows the validity of the adiabatic assumption (see Fig. 2). In the example simulation of Fig. 2, the driving frequencies are assumed to be an odd integer ratio (in this case, $\omega_x = \pi$ and $\omega_z = \pi/3$), which is a necessary condition for an open trajectory [26]. We also show that the direction of motion switches at phases that are integer multiples of $\pi/3$.

The first question we address is why flux reversal occurs when the initial phase is an integer multiple of $n\pi\omega_z/\omega_x$. To answer this question, we first look at the system properties when $\phi \neq n\pi\omega_z/\omega_x$. Let us consider the simulation conditions provided in Fig. 2. Since Eq. (8) is a periodic function, we can restrict our attention to one mutual time period, illustrated in Figs. 2(c)–2(e), from which it is clear there are three equal-length time segments of duration $T = \pi/\omega_x$. The function is single valued everywhere except at the end points of each time segment, $t = nT$, where ξ can assume the values of either 0 or π. By inspection of Fig. 2(d) (where $\phi < \pi/3$) it is clear that the first two segments are closed (meaning that the bead returns to its original position after the time interval). The closed intervals occur for $t \in 0 \ldots T$, and $t \in T \ldots 2T$. The last segment is an open monotonically increasing trajectory, occurring in the interval of $t \in 2T \ldots 3T$. This behavior can also be deduced mathematically from Eq. (8) by analyzing the solutions for ξ in the limits of $t = 0^+, T^-, T^+, 2T^-, 2T^+, 3T^-$, where the superscripts $(+, -)$ indicate that limits are taken from the right or left side, respectively. By contrast, an inspection of Fig. 2(d) (where $\phi > \pi/3$) reveals that the first and third intervals are closed, but the second interval is open
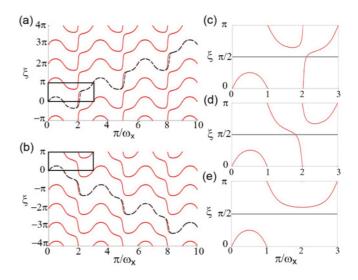

FIG. 2. (Color online) The comparison of numerical simulations (black dashed lines) with analytically computed trajectories (red solid lines) from Eq. (8) are shown to be in good agreement using initial phase differences of (a) $\phi = 0.3\pi$ and (b) $\phi = 0.4\pi$. The direction of motion switches at $\phi = \pi/3$. Parts (c) and (d) depict the bead motion of (a) and (b), respectively, over one mutual time period. Part (e) shows the bead motion is a closed trajectory at the phase transition point of $\phi = \pi/3$.

and monotonically decreasing. The direction of motion as a function of the initial phase can be determined by taking the time derivative of Eq. (8), yielding

$$\dot{\xi} = \frac{\omega_x \cos(\omega_x t) \sin(\omega_z t + \varphi) - \omega_z \sin(\omega_x t) \cos(\omega_z t + \varphi)}{\sin^2(\omega_x t) + \sin^2(\omega_z t + \varphi)}.$$

(9)

$$\pi \cos(2^+\pi)\sin(2^+\pi/3 + \varphi) - (\pi/3)\sin(2^+\pi)\cos(2^+\pi/3 + \varphi) > 0 \quad \text{for } \varphi < \pi/3,$$
$$\pi \cos(1^+\pi)\sin(1^+\pi/3 + \varphi) - (\pi/3)\sin(1^+\pi)\cos(1^+\pi/3 + \varphi) < 0 \quad \text{for } \varphi > \pi/3,$$

(10)

which shows the correct direction of motion for a given initial phase. This analysis is also true for any time point within the interval, which reveals that the open segments are monotonically increasing (or decreasing). When $\phi = \pi/3$, on the other hand, we observe the open and closed time segments merge together at a critical point satisfying $\tan(\xi) = 0/0$, and in this case the bead's composite trajectory is now closed [see Fig. 2(e)]. This analysis can be conducted for the other initial phases, where it is observed that the position of the open segment and its direction of motion will alternate with each increasing phase multiple of $\pi/3$. Furthermore, this analysis can be generalized to other frequency ratios.

We note that the above analysis is only applicable in the adiabatic limit (i.e., when the characteristic frequency is sufficiently large or the driving frequencies are sufficiently small) such that the bead always remains at a local potential energy minima. In order to characterize the deviation from the adiabatic limit, we plot the numerically calculated trajectory using the following driving frequencies: (i) $\omega_x = 0.01\omega_0^*$, (ii) $\omega_x = 0.1\omega_0^*$, and (iii) $\omega_x = \omega_0^*$, from which it is clear that higher driving frequencies lead to an overall time delay in the transition from the closed segment to the open segment, or vice versa (Fig. 3), however the general direction of motion does not change.

Case II. $\lambda_0/H_{\text{ext}} = O(1)$. Returning to our original equation, we now include the first static forcing term leading to the result

$$\dot{\xi} = \omega_0^*\{\cos(\xi)\sin(\omega_x t) - \sin(\xi)\sin(\omega_z t + \varphi) + \gamma \sin(2\xi)\},$$

(11)

where $\gamma = 2e^{-6\pi\beta}\lambda_0/H_{\text{ext}}$ is the static forcing coefficient. Here, our goal is to employ a combination of numerical simulations and perturbation analysis to explore the effect of the static forcing coefficient γ on the bead's trajectory. Using similar parameters as in case I (i.e., $\omega_x = \pi$, $\omega_z = \pi/3$, $\phi = 0.4\pi$), we present numerical simulations that reveal how the bead's trajectory changes as a function of γ, shown in Fig. 4. For low values $\gamma < 0.3$, the shape of the trajectory changes but the overall direction of motion remains the same (solid black lines in Fig. 4). Conversely, for high value $\gamma > 0.3$, the open and closed segments switch locations, and the overall bead trajectory is now in the opposite direction [blue (dashed) lines in Fig. 4]. We also observe that the open segment is no longer monotonically increasing. This phenomenon indicates

that the presence of a static forcing term can conceivably be used to induce two differential motions in two bead types (i.e., those that experience different static forcing terms on the same ratchet potential).

A qualitative explanation of this flux reversal behavior can be obtained by inspection of the time-varying potential energy landscape, shown in Fig. 5. Since adiabatic conditions are

As a simplifying example, we take the simulation conditions of Fig. 2 ($\omega_x = \pi$, $\omega_z = \pi/3$), and analyze the sign of the numerator of Eq. (9) during the open segment for the $\phi < \pi/3$ and $\phi > \pi/3$ phases, respectively. Here, we analyze just one time point near the left side of the open segment:
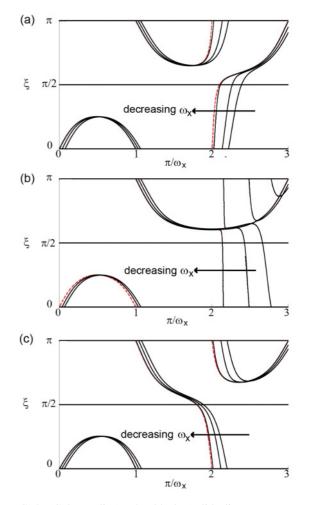

FIG. 3. (Color online) The black (solid) lines represent the numerically simulated trajectory for $\omega_x = 0.01\omega_0^*$, $\omega_x = 0.1\omega_0^*$, and $\omega_x = \omega_0^*$, and is compared against the red (dashed) lines which represent the analytical solutions for the conditions (a) $\phi < \pi/3$, (b) $\phi = \pi/3$, and (c) $\phi > \pi/3$.
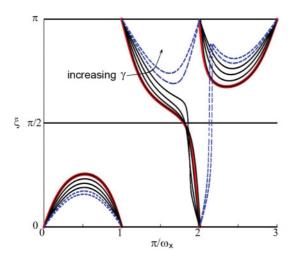
FIG. 4. (Color online) Numerically simulated bead trajectory as a function of increasing γ. The black (solid) lines show that for low values of γ the bead moves in the same direction as the $\gamma = 0$ simulations of Fig. 3, which is depicted as the red (thicker gray) line. The blue (dashed) lines show that for high values of γ, the open and closed segments switch and the bead now moves in an opposite direction, thereby demonstrating the influence of static forcing terms on the phase-dependent flux reversal.

assumed, the bead remains trapped at the local potential energy minima (indicated by the blue or black circles in Fig. 5). Clearly, the bead with a large static forcing term ($\gamma = 0.5$) remains trapped in a local potential energy minima at time $t = 1.6\pi/\omega_x$, which prevents it from escaping to the closest global energy minimum unlike the other bead with a smaller static forcing term ($\gamma = 0.2$). The local potential energy minima merges with a different global energy minima at a later time point, causing the bead with a larger static forcing term to move in the opposite direction of the bead with the smaller static forcing term. This effect is clearly visualized in the animation provided in the Supplemental Material [27], which is presented for $\phi = 0.4\pi$. In contrast, we also present Supplemental Material [27] (with $\phi = 0.3\pi$ and $\phi = 0.5\pi$, respectively), in which case all the beads move in the same direction.

Following the same procedure as in case I, under adiabatic assumptions we can derive an analytical relationship between the static forcing terms and the phase-induced flux reversal by setting Eq. (11) to equal zero, leading to the following expression:

$$\cos(\xi)\sin(\omega_x t) - \sin(\xi)\sin(\omega_z t + \varphi) + \gamma\,\sin(2\xi) = 0. \quad (12)$$

Due to the strong nonlinearity of Eq. (12), it is not possible to derive a complete solution; however, perturbation analysis can be used to analyze the system properties near the critical point where flux reversal takes place (i.e., $t \approx 2$, $\phi \approx \pi/3$, $\xi \approx \pi/2$). Using the following change of variables, $\phi = \pi/3 + \varphi$, $t = 2 + \tau$, and $\xi = \xi_0 + \varepsilon$, where φ, τ, and ε are small perturbations that can be either positive or negative, we find after simplification

$$\cos(\xi_0 + \varepsilon)\sin(\pi\tau) + \sin(\xi_0 + \varepsilon)\sin\left(\frac{\pi\tau}{3} + \varphi\right)$$
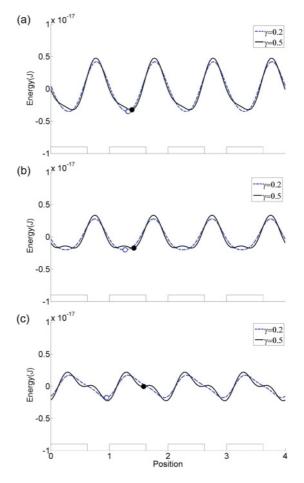$$+ \gamma\,\sin(2\xi_0 + 2\varepsilon) = 0. \quad (13)$$

FIG. 5. (Color online) Bead motion in a time-varying potential energy landscape. The blue (dashed) lines where $\gamma = 0.2$ and the black (solid) lines where $\gamma = 0.5$, depict the potential energy landscape for the time points: (a) $t = 1.6\pi/\omega_x$, (b) $t = 1.8\pi/\omega_x$, and (c) $t = 2\pi/\omega_x$, using the simulation parameters $\omega_x = \pi$, $\omega_z = \pi/3$, $\phi = 0.4\pi$, and $\omega_0^* = 50\omega_x$. The blue (open) circle and the black (closed) circle represent the numerically simulated locations of the $\gamma = 0.5$ and $\gamma = 0.2$ beads, respectively, at these three time points. The local potential energy barrier traps the bead with $\gamma = 0.5$ at time point (b) and causes it to move in the opposite direction of the bead with $\gamma = 0.2$.

The position $\xi_0 = \pi/2$ is analyzed because the bead must eventually transition through this point during the open segment, and the slope at this point indicates the direction of overall motion. Using the small angle approximation, we derive the following relationship:

$$\varepsilon = \left(\frac{\pi\tau}{3} + \varphi\right)(2\gamma + \pi\tau)^{-1}, \quad (14)$$

which indicates that the bead reaches the position $\xi_0 = \pi/2$ at a delayed time of $\tau = -3\phi/\pi$. When we analyze the slope near this critical time, we find that

$$\frac{d\varepsilon}{d\tau} = \frac{\pi}{3}\frac{1}{(2\gamma - 3\varphi)}, \quad (15)$$

which reveals that the slope will change based on the value of γ. When $\gamma < 3\varphi/2$, the direction of motion is positive, whereas when $\gamma > 3\varphi/2$, the direction of motion is negative. Thus, $\gamma = 3\varphi/2$ represents a direct analytical relationship
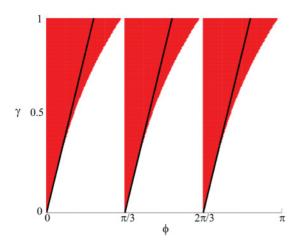
FIG. 6. (Color online) A separation window is presented to compare the direction of motion of a bead with and without static forcing terms. The red (shaded) regions indicate the phase and forcing conditions in which a bead having static terms moves in the opposite direction of one that does not. The white (unshaded) regions represent the conditions in which both beads move in the same direction. The black (solid) line is the analytically calculated separation boundary derived from Eq. (15).

of a bifurcation in the direction of the bead's motion. In Fig. 6, we provide a numerically computed phase diagram that compares the two cases (with and without static forcing terms) as a function of the phase ϕ. The red (shaded) regions depict the conditions in which the bead with static forcing terms moves in the opposite direction of one with no static forcing terms, whereas in the white (unshaded) regions both beads (those with vs without static forcing terms) move in the same direction. Additionally, we show that our analytical result $\gamma = 3\varphi/2$ adequately predicts the boundary of the separation window, particularly for low values of γ, where the perturbation analysis is more accurate.

Case III. Full analysis. We now extend to the full analysis with the goal of determining how the phase-induced flux reversal depends on the relative bead size, β, and thereby determine the experimental conditions for which two different bead types can move in opposite directions on the same ratchet potential. From Eq. (6) it is clear that β has the effect of changing the relative magnitude of the higher order forcing terms (both dynamic and static terms). For smaller beads (i.e., smaller β), the higher order terms decay less slowly than for the larger beads, requiring the inclusion of more terms to accurately model the substrate potential and forces on the bead. Additionally, the ratio of the static terms will also change relative to the dynamic terms, since the first static term is proportional to $e^{-8\pi\beta}$, whereas the first dynamic term is proportional to $e^{-2\pi\beta}$. Thus, the static forcing terms are expected to have a more pronounced effect on small beads (i.e., small β).

Using the assumption of an adiabatic limit by setting Eq. (6) to equal zero, we use the same perturbation analysis as in case II to solve for the location of the bead near the critical switching point. The result yields

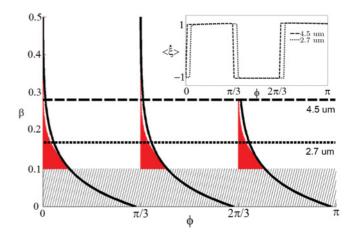$$\varepsilon = \frac{A(\pi\tau/3 + \varphi)}{\pi\tau B + C}, \quad (16)$$

FIG. 7. (Color online) A size-dependent separation phase diagram is presented for $\lambda_0/H_{\text{ext}} = 1$. The red (shaded) regions indicate the conditions in which a bead will move in the opposite direction of an infinitely large bead (i.e., one that has no static forcing terms), whereas in the white (unshaded) regions the two beads will move in the same direction. The shaded regions with $\beta < 0.1$ represent beads which are too small to move across the substrate and instead exhibit closed trajectories with zero time average velocity. An inset is presented to show the velocity vs phase behavior of the two 2.7 and 4.5 μm beads, which were tested experimentally, and are presented as dotted and dashed lines, respectively. The black (solid) lines are analytically derived separation boundaries of Eq. (19).

where A, B, and C are constants that depend on the bead size, β, given by

$$A = \sum_{j=0}^{\infty} (-1)^j (2j+1) f(j,\beta), \quad (17a)$$

$$B = \sum_{j=0}^{\infty} (-1)^j (2j+1)^2 f(j,\beta), \quad (17b)$$

$$C = \frac{8\lambda_0}{H_{\text{ext}}} e^{-6\pi\beta} \sum_{j=0}^{n} (-1)^j (j+1)^2 \frac{f(j,\beta) g(n,j,\beta)}{1 - g(n-1,n,\beta)}, \quad (17c)$$

where $f(j,\beta) = \cosh(4j\pi\beta) - \sinh(4j\pi\beta)$ and $g(j,n,\beta) = \cosh[8(n-j)\pi\beta] - \sinh[8(n-j)\pi\beta]$.

Like in case II, the bead reaches the position $\xi_0 = \pi/2$ at a delayed time of $\tau = -3\phi/\pi$. Thus, when we analyze the slope near this critical time point, we find that the bead velocity corresponds to the following relationship:

$$\frac{d\varepsilon}{d\tau} = \frac{A\varphi}{C - 3\varphi B}. \quad (18)$$

We thus conclude that the bifurcation defining the boundary of the separation window is given by

$$\varphi = \frac{C}{3B}. \quad (19)$$

Figure 7 presents the separation window for a range of bead sizes (here denoted by different values of β) compared with a fictitious infinitely large bead whose static forcing terms are negligibly small. The analytical and numerical solutions are in strong agreement. The inserted figure presents a comparison of the velocities of a 2.7 μm bead vs a 4.5 μm bead [denoted by black (dotted) and black (dashed) lines, respectively], which

are studied experimentally in Sec. IV. The results indicate that the prior experimental observations of opposite motion between two different bead types may have its origin in the influence of purely static forcing terms in the equations of motion.

IV. EXPERIMENTAL METHODS

A. Substrate fabrication

To create a permanent magnetization within the array, we developed high coercivity magnetic substrates, which are less susceptible to remagnetization in fields above 20 Oe than those used in our prior works. The fabricated magnetic thin film consists of a multilayer stack of 20 alternating layers of 9 Å Pt and 8 Å Co, with a 50 Å Ti base layer to improve adhesion, which is shown to resist remagnetization in external fields exceeding 100 Oe [28] The magnetic lattice was fabricated by conventional photolithographic lift-off technique using thin film deposition via molecular beam epitaxy (MBE) at the MBE Thin Film Deposition Service Center at North Carolina State University. In all experiments, the diameter of the magnets were $d_{\mathrm{M}} = 5.0\ \mu$m with lattice period $d = 8.0\ \mu$m.

B. Magnetic field control

The external field apparatus used to apply the multi-frequency fields is described in our prior works [14,15]. Briefly, two 6-cm-diameter solenoid coils with iron cores were arranged opposite of the chip to provide external uniform field along the x direction. An additional identical solenoid was placed below the chip to provide external uniform field along the z direction. An image of our experimental apparatus is provided in Fig. 8. In these experiments, the external magnetic fields were applied by passing electrical current through the solenoids. The fields were measured with a handheld Gaussmeter (Mz-201, Ming Zhe Tech) and we verified that the field variation was only a few percent across the chip. In all experiments, we applied a fixed frequency of 0.5 Hz (where
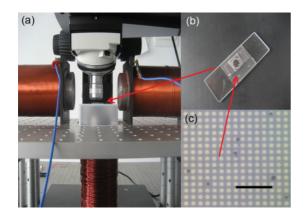

FIG. 8. (Color online) Experimental setup. (a) The sample is placed beneath an objective and two solenoid coils are positioned on either side of the chip to provide uniform fields in the x direction. An additional vertically oriented solenoid placed below the sample provides uniform field in the z direction. Image (b) depicts the microarray substrate on a glass slide. Image (c) depicts a microscopy image of a mixed suspension of 2.7 and 4.5 μm superparamagnetic beads resting on the microarray. The scale bar is 40 μm.

$\omega_x = 2\pi f_x$) to the horizontal coils and a fixed frequency of 1.5 Hz (where $\omega_z = 2\pi f_z$) to the vertical coil. The fields were controlled with a dual axis current controller (Cyberresearch card) and programmed with LABVIEW.

C. Experimental system

Magnetic beads with a mean diameter of 2.7 (Dynabeads M-270) and 4.5 (μm) (Dynabeads M-450) were purchased from Invitrogen Inc. The bead suspension is confined by a Secure-Seal spacer (9 mm in diameter and 0.12 mm in depth, Invitrogen Inc.) that was attached to the prepatterned magnetic substrate. All the experiments are performed at room temperature and the stock bead solution was diluted 100 fold with deionized water, having a viscosity of $\eta = 0.01$ P.

D. Video tracking and trajectory analysis

A LEICA DM LM microscope (Leica Microsystems) with 40× objective in bright field mode was used to image the experimental system. The experiments were recorded with a QIMAGING Retiga 2000R fast camera, and SimplePCI software (QCAPTURE PRO) was employed to record the trajectory of multiple beads simultaneously. IMAGE-PRO software (MediaCybernetics) was used for the postprocessing of the bead trajectories. We use a frame rate of five frames per second in order to capture the long-time average of bead trajectories over a large area. This was sufficient for capturing the details of the bead's motion, which had relatively small velocities, $V_0 = F_0/6\pi \eta a \sim 10\ \mu$m/s. Videos of the bead trajectories were taken at different phases and different external field amplitudes. From the videos, we analyzed the mean velocity and standard deviation of all the beads in each video. Beads that were smoothly moving to the right or left were recorded as having a dimensionless velocity of $+1$ and -1, respectively. Near the phase-modulated transition point, the beads velocities were averaged and the results are provided in Fig. 9.

V. EXPERIMENTAL RESULTS AND DISCUSSION

Figure 9 presents the time-averaged velocity of the beads as a function of the phase difference between the two driving fields, and for the three field strengths, 25, 50, and 100 Oe, respectively. The external field strength has the effect of change of the ratio $\lambda_0/H_{\mathrm{ext}}$, thereby allowing the static forcing coefficients to be adjusted. Figure 9(a) depicts the data for the 2.7 μm beads, and Fig. 9(b) for the 4.5 μm beads. The experiments revealed that the beads experienced flux reversal near the predicted phases of $\pi/3$, $2\pi/3$, and π. Reference lines at the phases of 60° and 120° are provided to highlight the delay in the phase shift of flux reversal. We observed that the phase delay of flux reversal increases as the field strength decreases, which is qualitatively consistent with the theoretical predictions on the influence of static forcing terms. Additionally, we verified that the phase delay was larger for the smaller beads, which again corresponds to the predicted theoretical trends. For example, the centers of the zero velocity for the 2.7 μm beads were (d) $\varphi = 5°$, 65°, and 124.5° for $H_{\mathrm{ext}} = 100$ Oe; (e) $\varphi = 9°$, 69°, and 129.5°, for $H_{\mathrm{ext}} = 50$ Oe; and (f) $\varphi = 12.5°$, 72°, and 132° for $H_{\mathrm{ext}} = 25$ Oe. The center of the zero-velocity region for the 4.5 μm beads was
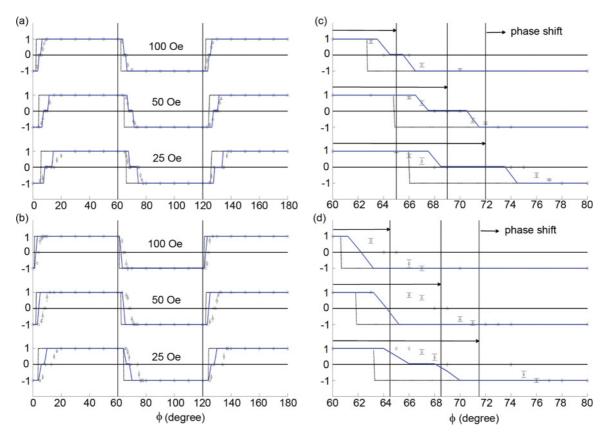
FIG. 9. (Color online) Experimental data is presented for the velocity of (a) 2.7 and (b) 4.5 μm beads as a function of the external driving field strength. Parts (c) and (d) present a magnified view of (a) and (b), respectively, near the phase $\pi/3$. The blue (solid gray) line is the simulated curve of a 2D point pole and the black (dotted) line is the analytical curve derived from the perturbation analysis. The arrows in parts (c) and (d) are provided to indicate the phase center of the zero-velocity region. These results show a minor shift in the phase center between the two bead types, and a more pronounced shift as a function of the driving field strength.

(a) $\varphi = 4°$, $64.5°$, and $123.5°$ for $H_{ext} = 100$ Oe, (b) $\varphi = 8.5°$, $68.5°$, and $128.5°$ for $H_{ext} = 50$ Oe, and (c) $\varphi = 11°$, $71.5°$, and $131°$, for $H_{ext} = 25$ Oe.

These results indicate that there is a region of approximately $1°$ where the two beads (2.7 and 4.5 μm beads, respectively) will experience differential motion. The Supplemental Material [27] shows the two cases in which either the big bead moves at the expense of the small bead or vice versa. The experimental window of separation was smaller than that predicted by theory in part due to the empirical discovery of a zero-velocity region that was not predicted in our perturbation analysis. The lack of agreement between theory and experiment could have a number of origins, including (1) oversimplification of the system as a 1D array of line poles; (2) the negligence of thermal motion, which may have prevented the beads from remaining in a local energy minima; or (3) oversimplification of the dipole forcing equation, since the beads are not in a region of uniform magnetic field where the dipole assumption is most accurate.

In order to explore these possible causes, we numerically simulated the motion of beads across several types of two-dimensional magnetic substrates, including (i) 2D array of point poles, (ii) 2D array of square magnets, and (iii) 2D array of circular magnets. First, we simulated the bead motion by including thermal fluctuations; however, since the potential

energy of the bead is many orders of magnitude larger than $k_B T$, the thermal effects were negligible and did not explain the origin of the zero-velocity region. We found that regardless of the initial position, the beads moved toward the centerline of the magnets ($y = 0$), which provides justification for the simplified 1D line pole model.

Interestingly, a zero-velocity region was found in numerical simulations only when the substrate magnetization was spatially asymmetric. For example, no zero-velocity region was found for substrates (i) and (ii) with equally sized magnets and gaps ($d_m/d = 0.5$); however, when the experimental parameters were simulated (5 μm magnets on an 8 μm period), a zero-velocity region was observed. Due to the spatial asymmetry of the circular magnets, the zero-velocity region was present in all simulated cases. The width of the zero-velocity region was independent of the driving frequency, which implies that this result occurs even in the adiabatic limit, and was found to predict the correct experimental trends with bead size and field strengths. Although there were minor differences among the three cases, the basic dynamic behavior was approximately the same and is more or less independent of the curvature of the magnets. Only spatial asymmetry was required to produce the correct results. Thus, in Fig. 9 we plot the numerical simulations obtained for a 2D point pole array [shown by the blue (solid) line] using spatial asymmetry of a

5 μm magnet on an 8 μm period, wherein the fitting parameter (substrate magnetization, with $\lambda_0 = 7.5$ Oe) was chosen to best match the experimental data of the 2.7 μm beads. Using perturbation, on the other hand, the zero velocity was never observed even for spatially asymmetric substrates [shown for comparison as the black (dotted) line in Fig. 9]. Interestingly, the phase shift from the perturbation analysis underpredicts the phase shift in numerical simulations. At present, we do not have a good explanation for why the perturbation analysis both fails to predict the presence of a zero-velocity region and underpredicts the phase shift, though it is likely due to the limitations of the asymptotic analysis.

Though numerical simulations could explain the presence of the zero-velocity region, the empirical separation window was still much smaller than was predicted by simulations (see Fig. 9). Specifically, for the experimental comparison of 4.5 μm beads with 2.7 μm beads, the numerical simulations predict a 3°–5° separation region, whereas in experiments we only observed a 1° separation region. One possible cause of this discrepancy is the oversimplification of the magnetic moment of the beads, which were assumed to be a point dipole defined by the field at the particle center. Since the 4.5 μm beads are roughly the same size as the magnets, the point dipole assumption breaks down when the field is highly nonuniform across the particle's volume. In other words, the fields and field gradients at the particle center are likely to be substantially lower than the volume-averaged fields of the 4.5 μm beads. This effect could have increased the static forcing terms of the 4.5 μm beads and would explain the smaller experimentally obtained separation window.

There could be several other reasons for the discrepancy between theory and experiment including time variation of the magnetization of the substrate, such as minor oscillation of the magnetization, adhesion, and other static or kinetic friction terms of the beads relative to the substrate. It is worth noting that the line pole model is a better description for experiments of bead motion on iron garnet films, in which the alternating up and down domains within the film are arranged in an array of parallel lines. In that case, opposite motion of two different bead types was observed [19].

Despite these challenges, the general experimental trends support the basic theoretical argument that static forcing terms can delay the phase at which beads experience flux reversal. The general scaling relationships for different bead sizes and field strengths are also consistent with this theory. Finally, the numerical simulations suggest that the best separation resolution can be achieved in a spatially symmetric lattice, which suggests that future experimental improvements can be realized to achieve opposite motion of two bead types on an array of micromagnets.

VI. CONCLUSION

Here, we use theory, simulation, and experiment to investigate the role of static forcing terms on the phase-induced flux reversal of beads in a multifrequency ratchet. Starting from the simplest theoretical model, we explore how flux reversal depends on the phase difference between two odd integer ratio driving frequencies, and we demonstrate that the addition of a static forcing term acts to delay the phase at which flux reversal is observed. We provide analytical results using perturbation analysis that captures the relationship between the static forcing terms and the phase of flux reversal, and we use the derived relationship to produce a theoretical separation window for two bead types that have different static forcing terms. Next, we extend this analysis to a more realistic model that indicates the possibility of moving two different bead types in opposite directions on the same ratchet. The perturbation analysis was able to qualitatively predict the correct trends of our experiments, including the scaling relationships with the bead size and the ratio between dynamic and static forcing terms. However, the perturbation analysis failed to explain the existence of a zero-velocity region, which was discovered both in experiments and in numerical simulations. The zero-velocity region was observed in numerical simulations only when the magnetic substrate was spatially asymmetric. Moreover, the scaling relationship of the width of the zero-velocity region was correctly predicted by the numerical simulations (i.e., the width increased with decreasing bead size and decreasing external field strength). These results serve to explain the prior experimental work on the motion of beads above field-modulated iron garnet films, and it also serves as a guide for future enhancements in our experimental system, including (i) the use of more symmetric substrate potentials and (ii) smaller beads relative to the magnet size. In conclusion, we have developed a framework for studying particle motion in multifrequency ratchets that shows the role of static forcing terms in the multiplexing capabilities of chip based magnetic separation systems. These results may also lead to insights on general ratchet behavior in other fields of physics.

ACKNOWLEDGMENT

[1] P. Hänggi, F. Marchesoni, and F. Nori, Ann. Phys. (N.Y.) **14**, 51 (2005).

[2] P. Hänggi and F. Marchesoni, Rev. Mod. Phys. **81**, 387 (2009).

[3] H. Linke, T. E. Humphrey, A. Löfgren, A. O. Sushkov, R. Newbury, R. P. Taylor, and P. Omling, Science **286**, 2314 (1999).

[4] D. Cole, S. Bending, S. Savel'ev, A. Grigorenko, T. Tamegai, and F. Nori, Nature Mater. **5**, 305 (2006).

[5] S. Ooi, S. Savel'ev, M. B. Gaifullin, T. Mochiku, K. Hirata, and F. Nori, Phys. Rev. Lett. **99**, 207003 (2007).

[6] S. Savel'ev, F. Marchesoni, P. Hänggi, and F. Nori, Phys. Rev. E **70**, 066109 (2004).

[7] M. V. Costache and S. O. Valenzuela, Science **70**, 066109 (2004).

[8] T. Salger, S. Kling, T. Hecking, C. Geckeler, L. Morales-Molina, and M. Weitz, Science **326**, 1241 (2009).

[9] R. Gommers, M. Brown, and F. Renzoni, Phys. Rev. A **75**, 053406 (2007).

[10] R. Gommers, S. Denisov, and F. Renzoni, Phys. Rev. Lett. **96**, 240604 (2006).

[11] S.-H. Lee, K. Ladavac, M. Polin, and D. G. Grier, Phys. Rev. Lett. **94**, 110601 (2005).

[12] A. Engel, H. W. Muller, P. Reimann, and A. Jung, Phys. Rev. Lett. **91**, 060602 (2003).

[13] S. Matthias and F. Muller, Nature (London) **424**, 53 (2003).

[14] L. Gao, N. Gottron III, L. Virgin, and B. B. Yellen, Lab Chip **10**, 2108 (2010).

[15] B. B. Yellen, R. M. Erb, H. S. Son, R. Hewlin Jr., H. Shang, and G. U. Lee, Lab Chip **7**, 1681 (2007).

[16] B. B. Yellen, O. Hovorka, and G. Friedman, Proc. Natl. Acad. Sci. U.S.A. **102**, 8860 (2005).

[17] A. R. Kose, B. Fischer, L. Mao, and H. Koser, Proc. Natl. Acad. Sci U.S.A. **106**, 21478 (2009).

[18] P. Tierno, S. V. Reddy, J. Yuan, T. H. Johansen, and T. M. Fischer, J. Phys. Chem. B **111**, 13479 (2007).

[19] P. Tierno, F. Sagues, T. H. Johansen, and T. M. Fischer, Phys. Chem. Chem. Phys. **11**, 9615 (2009).

[20] L. Cui, D. Holmes, and H. Morgan, Electrophoresis **22**, 3893 (2001).

[21] C.-F. Chou, O. Bakajin, S. W. P. Turner, T. A. J. Duke, S. S. Chan, E. C. Cox, H. G. Craighead, and R. H. Austin, Proc. Natl. Acad. Sci. U.S.A. **96**, 13762 (1999).

[22] J. S. Bader, R. W. Hammond, S. A. Henck, M. W. Deem, G. A. McDermott, J. M. Bustillo, J. W. Simpson, G. T. Mulhern, and J. M. Rothberg, Proc. Natl. Acad. Sci. **96**, 13165 (1999).

[23] A. van Oudenaarden and S. G. Boxer, Science **285**, 1046 (1999).

[24] M. Switkes, C. M. Marcus, K. Campman, and A. C. Gossard, Science **283**, 1905 (1999).

[25] A. Gopinathan and D. G. Grier, Phys. Rev. Lett. **92**, 130602 (2004).

[26] L. Gao, M. A. Tahir, L. N. Virgin, and B. B. Yellen, Lab Chip **11**, 4214 (2011).

[27] See Supplemental Material at http://link.aps.org/supplemental/10.1103/PhysRevE.85.041407 for movies.

[28] O. Hellwig, T. Hauet, T. Thomson, E. Dobisz, J. D. Risner-Jamtgaard, D. Yaney, B. D. Terris, and E. E. Fullerton, Appl. Phys. Lett. **95**, 232505 (2009).